

Dynamical topological phase transition in cold Rydberg quantum gases

Jun Zhang^{1,2,*}, Ya-Jun Wang^{1,2,*}, Bang Liu^{1,2}, Li-Hua Zhang^{1,2}, Zheng-Yuan Zhang^{1,2}, Shi-Yao Shao^{1,2}, Qing Li^{1,2}, Han-Chao Chen^{1,2}, Yu Ma^{1,2}, Tian-Yu Han^{1,2}, Qi-Feng Wang^{1,2}, Jia-Dou Nan^{1,2}, Yi-Ming Yin^{1,2}, Dong-Yang Zhu^{1,2}, Bao-Sen Shi^{1,2}, and Dong-Sheng Ding^{1,2,†}

¹Key Laboratory of Quantum Information, University of Science and Technology of China, Hefei, Anhui 230026, China. and

²Synergetic Innovation Center of Quantum Information and Quantum Physics, University of Science and Technology of China, Hefei, Anhui 230026, China.

(Dated: September 18, 2024)

Study of phase transitions provide insights into how a many-body system behaves under different conditions, enabling us to understand the symmetry breaking, critical phenomena, and topological properties. Strong long-range interactions in highly excited Rydberg atoms create a versatile platform for exploring exotic emergent topological phases. Here, we report the experimental observation of dynamical topological phase transitions in cold Rydberg atomic gases under a microwave field driving. By measuring the system transmission curves while varying the probe intensity, we observe complex hysteresis trajectories characterized by distinct winding numbers as they cross the critical point. At the transition state, where the winding number flips, the topology of these hysteresis trajectories evolves into more non-trivial structures. The topological trajectories are shown to be robust against noise, confirming their rigidity in dynamic conditions. These findings contribute to the insights of emergence of complex dynamical topological phases in many-body systems.

The phase in topology reveals the inherent space property that is preserved under continuous deformations, such as stretching and bending. Topological phase transitions refer to changes in the state of matter that are characterized by alterations in the topological properties of the system, rather than conventional symmetry-breaking mechanisms [1–5]. Studying topological phases and their transitions involves exploring materials’ features with distinct global geometric features and investigating how these phases change under different conditions [6–9]. These transitions can occur between different topological phases, where the properties of the system remain invariant under continuous transformations but differ in their topological invariants [10–12], such as the presence of edge states [13–15], topological insulators [16–18] and superconductors [19, 20] in quantum systems. In addition, the topological phase transitions are also investigated in a non-equilibrium system [21, 22], non-Hermitian system [23–26], and dynamical

systems [27–30], in which dynamical behaviors and interactions enrich topological properties.

Due to the exaggerated properties of Rydberg atoms [31–33], they not only enhance the complexity of the system’s behavior but also provides a platform for investigating topological states and their phase transitions, for example, topological band structure [14] and topological order in the Kagome lattice [34], and other exotic topological features [35–38]. The characteristic long-range interaction makes the laser-driven Rydberg atomic system displaying rich non-equilibrium physics and nonlinear dynamics [39–56]. The interactions in Rydberg atoms induce non-Hermitian properties [57] and hysteresis loops characterized by asymmetrical responses to varying probe intensities [58]. The ability to precisely control the excitation of Rydberg atoms using external microwave fields enables us to create effective Hamiltonians that exhibit rich dynamical evolution; and this helps us to investigate how dynamical topological phases emerge over system parameters.

In this work, we observe dynamical topological phase transition in cold Rydberg quantum gases. We focus on how the interplay between interactions and external microwave fields gives rise to rich topological structures. By increasing the intensity of microwave field, the probe transmission behaves various hysteresis trajectories, particularly the corresponding winding number flips across the critical point due to the eigenvalue ‘gap-closing’. During the flipping process, a non-trivial intermediate state emerges from the spontaneously breaking of particle-hole symmetry, characterized by two opposite winding trajectories. The robustness of these topological trajectories against noise indicates their rigidity under dynamic conditions. This stability is closely related to topological invariants, which describe the winding number of the hysteresis loops remain unchanged despite perturbations. Studying the topological features of dynamical evolution trajectories in Rydberg atom systems serves as a valuable reference for understanding topology and its’ evolution in many-body scenarios.

Physical model

To investigate the dynamical topological phase transition, we consider an interacting four-level Rydberg

* J.Z and Y.J.W contribute equally to this work.

† dds@ustc.edu.cn

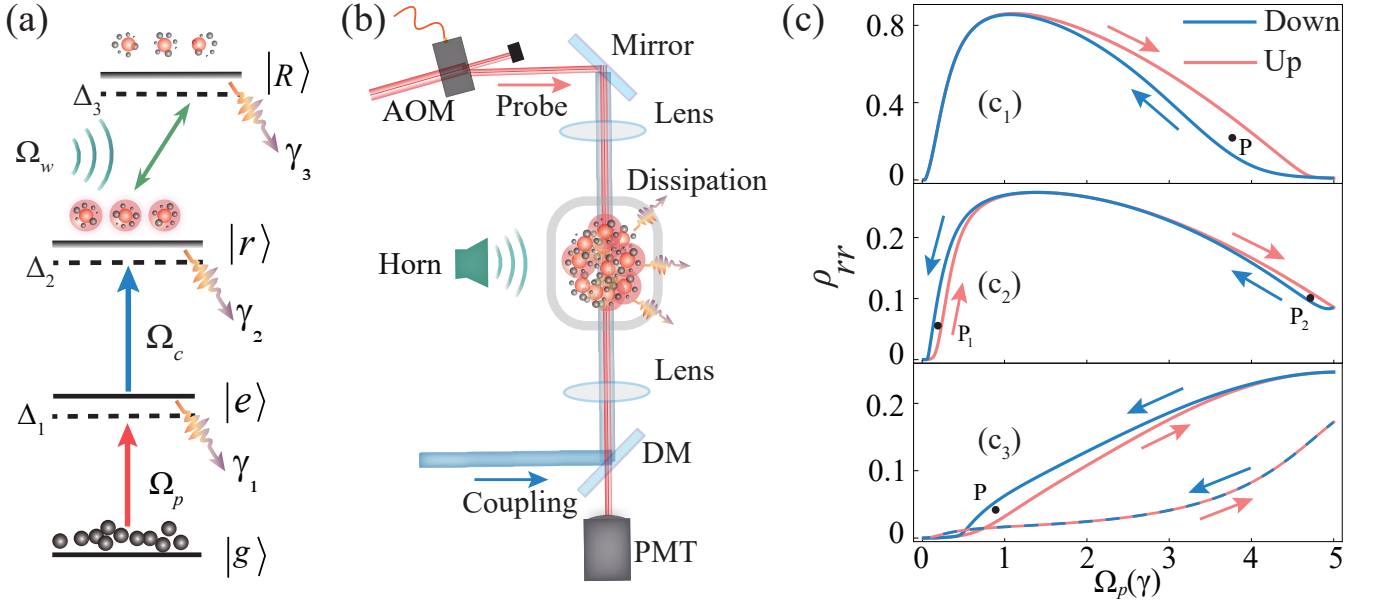


Figure 1. **Schematic of dynamical topological phase transition.** (a) Energy level diagrams. Probe and coupling fields excite atoms from the ground state $|g\rangle$ to the Rydberg state $|r\rangle$, and a microwave field drives the transition $|r\rangle \leftrightarrow |R\rangle$. (b) Schematic diagram of the experimental setup. The probe beam is incident opposite to the coupling beam and focused in cold ^{85}Rb atoms. A horn radiates microwave electric field on atoms. MW: microwave, AOM: acousto-optic modulator, PMT: photomultiplier tube, DM: dichroic mirror. (c) The plotted hysteresis trajectories of population ρ_{rr} under microwave Rabi frequency $\Omega_{mw} = 0.1 \gamma$ (c_1), $\Omega_{mw} = 2.2 \gamma$ (c_2), and $\Omega_{mw} = 5.5 \gamma$ (c_3). The dashed lines in (c_3) represents the hysteresis trajectory under the condition $V = 0$, which exhibits the same evolution trajectories with no loops. The pink and blue arrows represents the positive and negative scanning Ω_p , respectively. The black points P , P_1 , and P_2 are the references used for calculating the winding number.

atomic system as illustrated in Fig. 1(a). The system consists of four atomic state manifolds: the ground state $|g\rangle$, the intermediate excited state $|e\rangle$, the Rydberg state $|r\rangle$, and another Rydberg state $|R\rangle$. The probe field with Rabi frequency (detuning) Ω_p (Δ_1) drives the transition $|g\rangle \leftrightarrow |e\rangle$. The coupling field, with Rabi frequency Ω_c and detuning Δ_2 , couples the transition $|e\rangle \leftrightarrow |r\rangle$. Additionally, the microwave field with Rabi frequency (detuning) Ω_{mw} (Δ_3) drives the transition $|r\rangle \leftrightarrow |R\rangle$. The spontaneous decay rates for the states $|e\rangle$, $|r\rangle$ and $|R\rangle$ are γ_1, γ_2 and γ_3 , respectively. The experimental setup is depicted by Fig. 1(b). In this framework, the Hamiltonian in the interaction picture and rotating-wave approximation is

$$\begin{aligned}
 H = & \sum_j \left[\left(\frac{\Omega_p}{2} |e\rangle \langle g|_j + \frac{\Omega_c}{2} |r\rangle \langle e|_j + \frac{\Omega_{mw}}{2} |R\rangle \langle r|_j \right) + H.c. \right] \\
 & - \sum_j (\Delta_1 |e\rangle \langle e|_j + \Delta_r |r\rangle \langle r|_j + \Delta_R |R\rangle \langle R|_j) \\
 & + V \sum_{j < k} |r\rangle \langle r|_j \otimes |r\rangle \langle r|_k,
 \end{aligned} \tag{1}$$

where $\Delta_r = \Delta_1 + \Delta_2$ represents two-photon detuning and $\Delta_R = \Delta_1 + \Delta_2 + \Delta_3$ corresponds to three-photon detuning. V represents the dipole-dipole interaction strength between Rydberg atoms. The interactions between atoms in the states $|r\rangle$ influence the many-body

quantum dynamics. To explore the underlying physics of this dynamical process, we employ the mean-field approximation. Here, the interactions induce an additional dissipation on the state $|r\rangle$, resulting in a non-Hermitian Hamiltonian [58]. The eigenvalue trajectories on the complex plane display a ‘gap-closing’ topological characteristics indicating the particle-hole symmetry breaking, see detailed information in Methods section. In this case, the system dynamics of adding Rydberg atoms to the system is not equivalent to removing Rydberg atoms.

In mean-field treatment of $\gamma_2 \rightarrow \gamma + V\rho_{rr}$ [here ρ_{rr} is the population of atoms on the state $|r\rangle$], we solve the time-dependent evolution of system employing the Lindblad master equation as follows

$$\frac{\partial \rho(t)}{\partial t} = -i[H(t), \rho(t)] + \sum_i (L_i \rho(t) L_i^\dagger - \frac{1}{2} \{L_i^\dagger L_i, \rho(t)\}). \tag{2}$$

We investigate the loop trajectory of the population ρ_{rr} by performing both forward (Up) and backward (Down) scans of the probe field Rabi frequency Ω_p , as depicted in Fig. 1(c). The interactions between Rydberg atoms break the symmetry of system and give rise to a non-closed hysteresis trajectories [58]. As the microwave Rabi frequency Ω_{mw} increases, the trajectories of ρ_{rr} exhibit different patterns, as illustrated in Figs. 1(c1), (c2) and

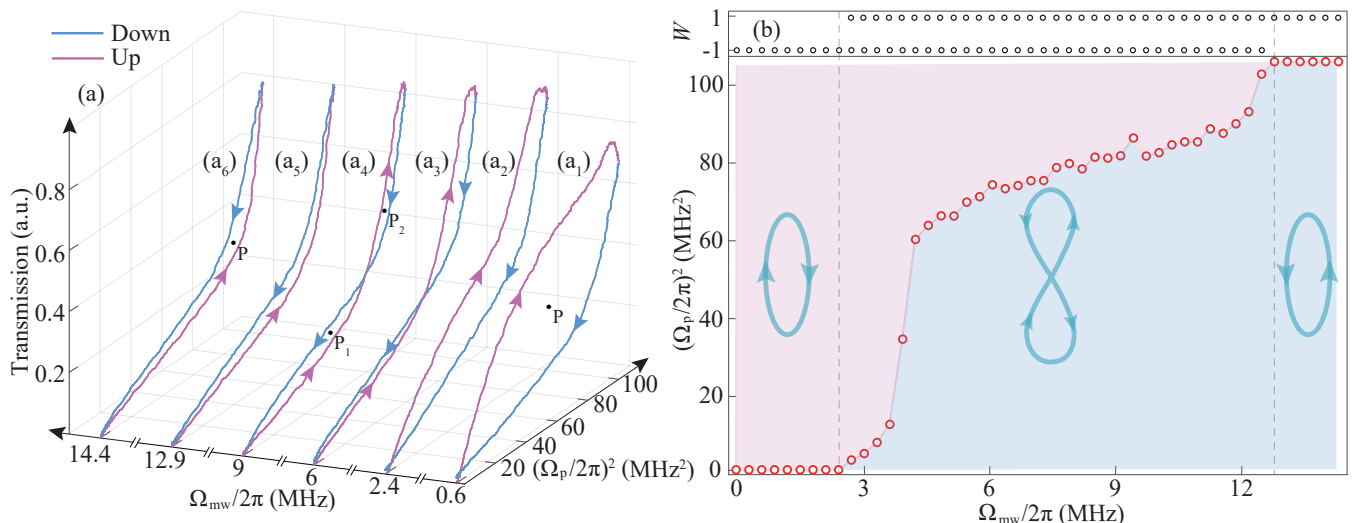


Figure 2. **Measured phase diagram.** (a) Measured hysteresis trajectories of probe transmission versus the microwave Rabi frequency Ω_{mw} . At low Ω_{mw} , the hysteresis trajectories consistently exhibit a clockwise direction, characterized by a winding number of $W = -1$, as illustrated in panels (a₁) and (a₂). As Ω_{mw} increases, the topological properties of the hysteresis trajectories begin to change, leading to intertwined rotation direction under varying $(\Omega_p/2\pi)^2$, as shown in (a₃) and (a₄). With further increases in Ω_{mw} , the hysteresis trajectories reverse direction to become anti-clockwise, resulting in a winding number of $W = 1$, as shown in (a₅) and (a₆). The black points P , P_1 , and P_2 are the references used for calculating the winding number. (b) The measured phase diagram of the winding number W is plotted against $\Omega_{mw}/2\pi$ and $(\Omega_p/2\pi)^2$. In this diagram, the pink area indicates that the winding number W of the hysteresis trajectory is -1, while the blue area corresponds to a winding number of $W = 1$, see the up panel of (b). The red circles represent the intersection points between the Up and Down processes in the phase transition. The different winding structures marked by the blue curves display distinct topology.

(c3), which correspond to distinct dynamic phases of system. To distinguish these dynamic phases and characterize their topological features, we define a winding number, expressed as follows:

$$W = \frac{1}{2\pi} \int_C \frac{(\Omega_p - x_0) \dot{\rho}_{rr} dt - (\rho_{rr} - y_0) \dot{\Omega}_p dt}{(\Omega_p - x_0)^2 + (\rho_{rr} - y_0)^2}, \quad (3)$$

it quantifies the number of times a system's winding around a reference point (x_0, y_0) . A winding number of $W = -1$ indicates that ρ_{rr} evolves clockwise with respect to Ω_p in the parameter space, while conversely, $W = 1$ signifies a counterclockwise evolution. In our simulations, the winding numbers are $W = -1$ in Fig. 1(c1), $W = 1$ in Fig. 1(c3), and a coexistence of $W = 1$ and $W = -1$ in Fig. 1(c2), where each reference point of P , P_1 , and P_2 in the loops is considered separately. The transition of the winding number from $W = 1$ to $W = -1$ as varying Ω_{mw} indicates a dynamical topological phase transition. During the phase transition, a critical point occurs where the trajectory of ρ_{rr} is folded, resulting in the coexistence of $W = 1$ and $W = -1$, as depicted in Fig. 1(c2).

Phase diagram

To investigate the dynamical topological phase transition, we conduct experiments with a cold ensemble of ⁸⁵Rb atoms utilizing electromagnetically induced trans-

parency (EIT). The system dynamics are monitored by measuring probe transmission. We modify the probe intensity using a triangle waveform, generated by an acousto-optic modulator with a sweep period of T_s , and record the transmission trajectories during both the Up and Down processes. Due to the interactions between Rydberg atoms, the induced-dissipation plays a vital role in the system dynamic evolution. The increase and decrease of Rydberg atoms [by scanning Ω_p^2] result in asymmetrical responses to probe transmission, leading to hysteresis loop [58]. In the experiment, we employ a microwave field to alter the atoms' dynamical evolution and introduce an additional nonlinearity into the system.

Through varying the microwave Rabi frequency Ω_{mw} , we observe the distinct hysteresis trajectories, as shown in Fig. 2(a). When Ω_{mw} is small [$\Omega_{mw}/2\pi \leq 2.4$ MHz], the hysteresis trajectories exhibit a clockwise evolution, resulting in a winding number is $W = -1$ [Figs. 2(a₁) and (a₂)]. While for $\Omega_{mw}/2\pi \geq 12.6$ MHz, the hysteresis trajectories evolve in a counterclockwise direction with a winding number of $W = 1$, as shown in Figs. 2(a₅) and (a₆). For $2.4 \text{ MHz} < \Omega_{mw}/2\pi < 12.6$ MHz, the hysteresis trajectories become folded and intersect, the resulting interlaced curve displays coexisting winding numbers of $W = -1$ and $W = 1$ by considering the reference points P_1 and P_2 respectively, as illustrated in Figs. 2(a₃) and (a₄). This unique topological configuration is particularly intriguing because it signifies a pair opposite winding numbers, revealing the complexities in many-body

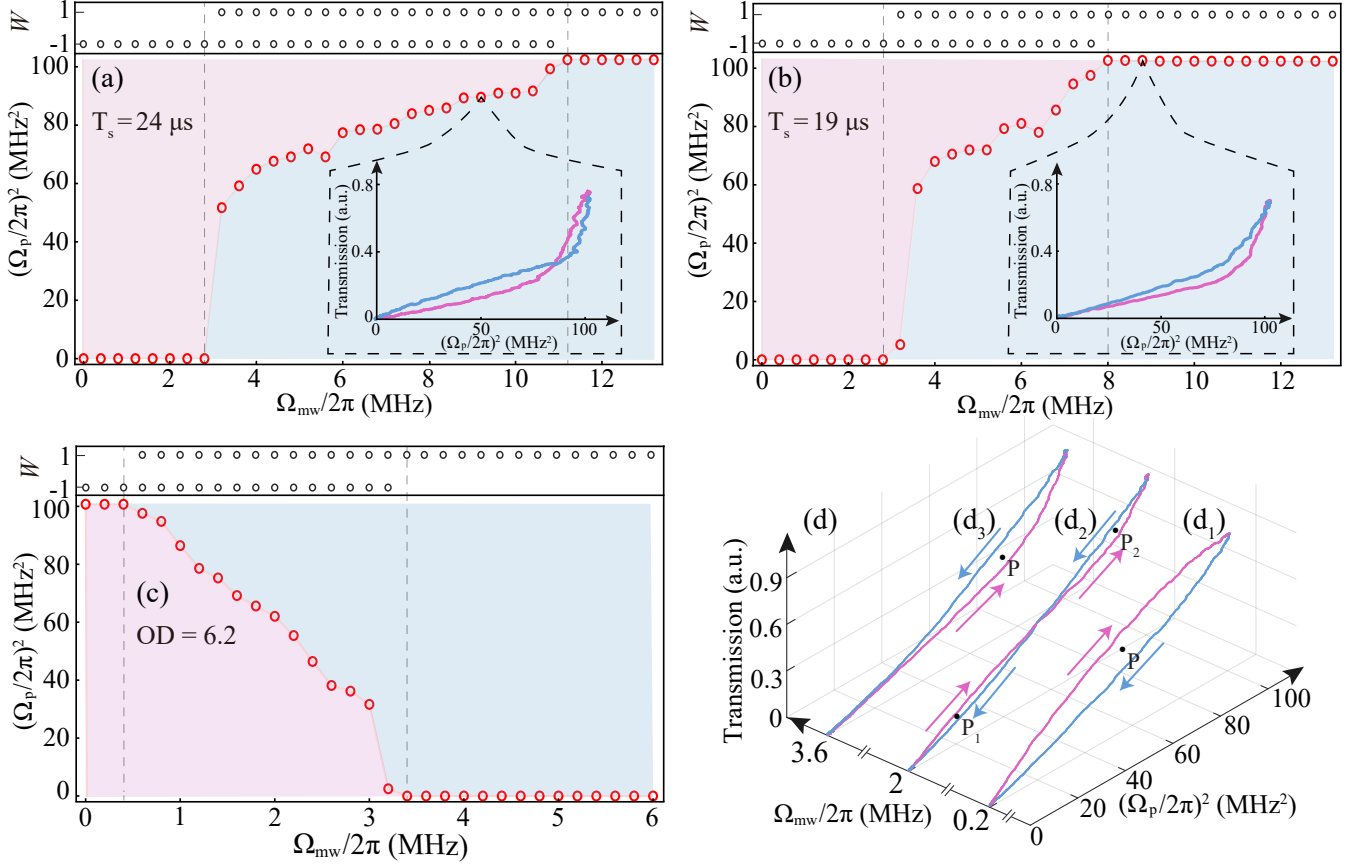


Figure 3. **Winding dynamics and reverse folded trajectories.** (a) Measured phase diagram of winding number W versus $\Omega_{mw}/2\pi$ and $(\Omega_p/2\pi)^2$ under $T_s = 24 \mu\text{s}$ (a) and $T_s = 19 \mu\text{s}$ (b). The up panels correspond to the measured winding numbers of hysteresis trajectories. According to the measured phase diagrams, the winding number flipping range for case of $T_s = 24 \mu\text{s}$ (a) is larger than that for $T_s = 19 \mu\text{s}$ (b). The subfigures in (a) and (b) show the measured hysteresis trajectories under the same microwave Rabi frequency $\Omega_{mw}/2\pi = 8.8 \text{ MHz}$. In these processes, the optical density is set as $\text{OD} = 7.5$ during measurement. (c) Measured phase diagram and winding number W versus $\Omega_{mw}/2\pi$ and $(\Omega_p/2\pi)^2$ under the conditions $\text{OD} = 6.2$ and $T_s = 15 \mu\text{s}$. (d₁) is the measured hysteresis trajectories at the microwave Rabi frequency $\Omega_{mw}/2\pi = 0.2 \text{ MHz}$. Similarly, (d₂) corresponds to measurement at $\Omega_{mw}/2\pi = 2 \text{ MHz}$, and (d₃) corresponds to measurement at $\Omega_{mw}/2\pi = 3.6 \text{ MHz}$. The black points P , P_1 , and P_2 are the references used for calculating the winding number.

systems.

The measured hysteresis trajectories as a function of Ω_{mw} enable us to map the full dynamics in the parameter space of $(\Omega_p/2\pi)^2$ and $\Omega_{mw}/2\pi$. By recording the intersection points between the Up and Down processes, we uncover the dynamical topological phase transition, as illustrated in Fig. 2(b). The phase diagram reveals three distinct phases, each characterized by its winding number.

The role of the microwave field here is to build a population transfer channel between the Rydberg states $|r\rangle$ and $|R\rangle$, breaking the three-level EIT configuration. Thus, with a strong microwave field, the absorption of probe field becomes dominant. This can also be revealed by the real parts of the eigenvalue E_3 as shown in Fig. 5(c) in Methods section [the E_3 characterizes the Rydberg state $|r\rangle$]. The combination of population transfer and interaction-induced dissipation destroys the EIT

coherence, thus leading to the decrease of transmission. Conversely, when Ω_p^2 is reduced, the interaction-induced dissipation is alleviated, leading to a relative decrease in absorption within the system. These result in an opposite winding number by comparing with the scenario involving a weak microwave field.

Winding dynamics

In the dynamical topological phase transition, the system undergoes a critical process of flipping the winding number. To study the dynamics of the winding number flipping, we chose two different time scales and measure the winding number versus Ω_{mw} . In the experiment, we measure the phase diagram versus $\Omega_{mw}/2\pi$ and $(\Omega_p/2\pi)^2$ at the time scales of $T_s = 24 \mu\text{s}$ [Fig. 3(a)] and $T_s = 19 \mu\text{s}$ [Fig. 3(b)], respectively. At $T_s = 24 \mu\text{s}$, the system un-

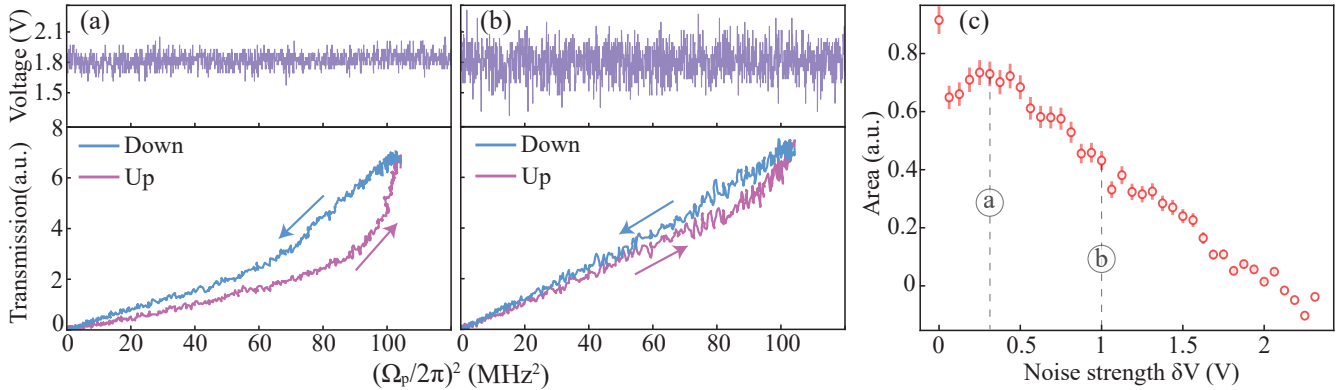


Figure 4. **Robustness against fluctuations.** (a) and (b) Single experimental runs for noise strength indicated in (c). The up panels present the voltage fluctuations loaded on the acousto-optic modulator, which induces fluctuations on the probe field detuning. The down panels correspond to the measured hysteresis loops. (c) The closed area of the Down and Up processes as a function of noise strength $\delta V = V_{max} - V_{min}$, here V_{max} and V_{min} correspond to the maximal and minimal voltage.

dergoes a dynamical topological phase transition over folded transmission trajectories with a larger parameter range [$2.8 \text{ MHz} < \Omega_{mw}/2\pi < 11.2 \text{ MHz}$], while at $T_s = 19 \mu\text{s}$, the phase transition occurs within a smaller parameter range [$2.8 \text{ MHz} < \Omega_{mw}/2\pi < 8.0 \text{ MHz}$]. We also find that the variation of the intersection point in the intermediate state to the microwave Rabi frequency Ω_{mw} is more sensitive at a relative small time scale.

The underlying reason for this effect is that interaction-induced dissipation—arising from the accumulation of interactions over time—affects the coherence of Rydberg atoms and varies their response to the probe field. A relatively long (or short) time interval ΔT leads to a big (small) number of accumulated Rydberg atoms, resulting in strong (weak) interactions. Specifically, in the case of a longer time interval, a stronger microwave field is required to flip the winding number, as shown in Fig. 3(a). This is because that the strong dissipation on the Rydberg state $|r\rangle$ is easier to fold the transmission trajectory. The insets in Figs. 3(a) and (b) show the results of single measurement conducted under the same parameter of $\Omega_{mw}/2\pi = 8.8 \text{ MHz}$. For $T_s = 24 \mu\text{s}$, the system remains in the intermediate state during the topological phase transition, resulting from a broader flipping range.

Reverse folded trajectories

In the experiment, we investigate the dynamics of the topological phase transition under low optical density ($\text{OD} = 6.2$). The corresponding phase diagram is presented in Fig. 3(c). We observe that the intersection point between the Up and Down processes moves from higher to lower values of $(\Omega_p/2\pi)^2$, a significant departure from the behavior observed at relatively high OD, as seen in the phase diagrams of Fig. 2(b) or Figs. 3(a) and (b). Specially, during the intermediate state of the phase

transition, the winding number W changes depending on the regime of $(\Omega_p/2\pi)^2$: it takes a value of $W = -1$ in the regime of larger $(\Omega_p/2\pi)^2$ and flips to $W = 1$ in the regime of smaller $(\Omega_p/2\pi)^2$, as illustrated in Fig. 3(a).

We present three examples of hysteresis trajectories to illustrate the differences, as shown in Fig. 3(d). At a low microwave Rabi frequency of $\Omega_{mw}/2\pi = 0.2 \text{ MHz}$, the system is characterized by a winding number of $W = -1$. As $\Omega_{mw}/2\pi$ increases to 2 MHz , the system enters an intermediate state, depicted in Fig. 3(d₂). In this figure, the hysteresis trajectories of the Down and Up processes fold and exhibit opposite topological patterns by comparing with the results given in the subfigure in Fig. 3(a) (or Figs. 2(a₃) and (a₄)). By considering the reference points P_1 and P_2 , the winding number is $W = -1$ and $W = 1$, respectively. At $\Omega_{mw}/2\pi = 3.6 \text{ MHz}$, the winding number of the hysteresis trajectories changes to $W = 1$ [Fig. 3(d₃)].

Noise-resistant topological properties

The winding number corresponds to a topological invariant of system, which remains unchanged under continuous deformations of the system. This means that even if the system experiences fluctuations (e.g., the fluctuation of probe detuning Δ_p), the fundamental properties associated with these topological invariants persist. In the experiment, we measure the hysteresis loops against the amplitude of the probe detuning fluctuation $\sim \delta V$ and investigate the stability of dynamical topological invariant. The measured results are given in Fig. 4.

We measure the hysteresis trajectories under weak fluctuations (Fig. 4(a)) and strong fluctuations (Fig. 4(b)), and find that the system is robust to noise and still remains in the same phase (the winding number is $W = 1$). To further display the robustness of dynamical topology

against noise, we plot the closed-loop area of the hysteresis loops under various fluctuation amplitude δV . When the fluctuation amplitude is extremely weak, the area scarcely decreases, suggesting that the system is immune to fluctuations. However, as the amplitude of the fluctuations increases, the transmission trajectory is affected, leading to a linear decrease in the area with respect to δV . Despite this change, the winding number remains unchanged, exhibiting the rigidity of topological phase.

Conclusion

By varying the microwave Rabi frequency, Ω_{mw} , and the sweep time, T_s , the rich dynamics of topological features for the intermediate state have been investigated. The highly sensitive variation of the intersection point to the microwave field Rabi frequency Ω_{mw} [see Fig. 2(b), the intersection rises rapidly as we increase Ω_{mw}] can be used for critical enhanced metrology. Studying the dynamics of the winding number flipping and the scaling of intersection point is essential for unraveling the interplay between topology and dynamics in Rydberg many-body systems, offering precisely control technology to change topological characteristics.

In summary, we have observed complex dynamical topological trajectories emerging from the interplay of strong long-range interactions among Rydberg atoms and a microwave field. Specifically, we have investigated dynamic topological phase transitions where the winding number of the hysteresis loop evolves from -1 to 1. The intermediate transition states associated with the distinct folded topological trajectories are observed and display different dynamics by varying the sweep time and the atomic density. Furthermore, we demonstrate an experiment illustrating the robustness of topology against fluctuations, revealing the property of topological invariant of system. These intriguing results have sparked the exploration of the underlying physical mechanisms behind the topological phase transition and the dynamic evolution in quantum many-body system.

METHODS

Details of the experimental setup

To study the emergence of dynamical topological phase transition, we prepare a cold ensemble of ^{85}Rb atoms trapped in a three-dimensional magneto-optic trap. The atomic ensemble is prepared in the ground state $|g\rangle = |5S_{1/2}, F=3\rangle$ by an optical pumping process. In our experiment, we shield the magneto-optical trap with a double-layer magnetic shielding system. This setup effectively shields the system from external magnetic fields and lowers the internal magnetic field to below 10 mGauss. This configuration can avoid the dephasing from the earth's magnetic field.

We used a two-photon transition scheme to excite ^{85}Rb atoms from the ground state to the Rydberg state. The probe beam ($\omega_p \approx 10 \mu\text{m}$) drives the atoms from the ground state $|g\rangle$ to the intermediate excited state $|e\rangle = |5P_{3/2}, F=4\rangle$, and the coupling beam ($\omega_c \approx 20 \mu\text{m}$) then drives the transition from $|e\rangle$ to the Rydberg state $|r\rangle = |47D_{5/2}\rangle$. We used a near-resonant microwave electric field to drive the RF transition between the two different Rydberg states of $|r\rangle$ and $|R\rangle = |46F_{7/2}\rangle$ with a frequency of $2\pi \times 22.55 \text{ GHz}$. The microwave electric field used in our experiment was generated by a radio-frequency source and a horn antenna, as shown in Fig. 1(a) in the main text. The probe beam and coupling beam are focused into the cold atomic ensemble, and the transmittance of the EIT is obtained by detecting the intensity of the probe beam via a photo-multiplier Tube.

In experiment, we loaded a triangular waveform that was generated using a signal generator (RIGOL DG4102) onto the acousto-optic modulator. The functional form of the triangular wave signal is $V(\tau) = 6(1/2 - |\tau/T_s - 1/2|)$, where the T_s represents the period time of one scan cycle and $0 \leq \tau \leq T_s$. By this way, we produce the process of increasing $(\Omega_p/2\pi)^2$ from 0 MHz^2 to 102.4 MHz^2 (Up process) and the process of decreasing $(\Omega_p/2\pi)^2$ from 102.4 MHz^2 to 0 MHz^2 (Down process).

The eigenvalue trajectories

Due to the distance-dependent van der Waals (vdW) potential $V_{\text{vdW}} \propto C_6/R^6$ among Rydberg atoms, this gives rise to an effective dissipation rate γ_{eff} on state $|r\rangle$. Thus, the resulting effective non-Hermitian Hamiltonian is expressed as:

$$H = \sum_j \left[\left(\frac{\Omega_p}{2} \sigma_{eg}^j + \frac{\Omega_c}{2} \sigma_{gr}^j + \frac{\Omega_{mw}}{2} \sigma_{rR}^j \right) + H.c. \right] - \sum_j \left[\Delta_1 \sigma_{ee}^j + (\Delta_r + i\gamma_{\text{eff}}) \sigma_{rr}^j + \Delta_R \sigma_{RR}^j \right] \quad (4)$$

where $\sigma_{ab}^j = |a_j\rangle \langle b_j|$ ($a, b = g, e, r, R$), $\Delta_r = \Delta_1 + \Delta_2$ and $\Delta_R = \Delta_1 + \Delta_2 + \Delta_3$. $\gamma_{\text{eff}} = \frac{V_{\rho_{rr}}}{2}$ is the interaction-induced dissipation term from the mean-field treatment, which essentially broadens the energy level $|r\rangle$ [58].

This non-Hermitian Hamiltonian has particle-hole symmetry

$$\mathcal{C}H^*\mathcal{C}^\dagger = -H, \quad (5)$$

where $\mathcal{C} = \mathcal{I} \otimes \sigma_z \mathcal{K}$, \mathcal{I} is the identity matrix, σ_z is the Pauli matrix, and \mathcal{K} is the complex conjugation. When the microwave Rabi frequency Ω_{mw} varied, the system's particle-hole symmetry is spontaneously broken, leading to a topological phase transition. By setting the detunings $\Delta_1 = \Delta_2 = \Delta_3 = 0$, we calculate the eigenvalues of the above non-Hermitian Hamiltonian, denoted as $E_1 \sim E_4$. Then, we obtain the real and imaginary

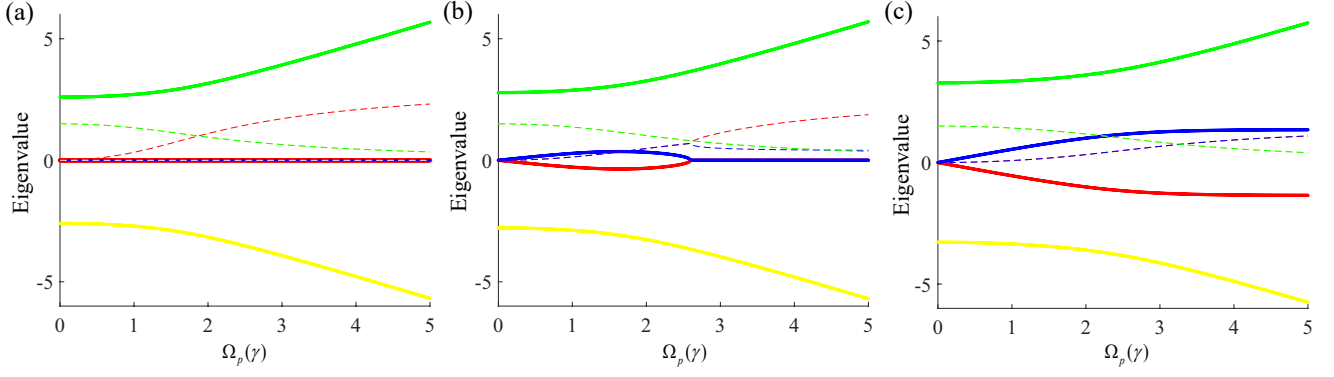


Figure 5. **The Energy spectrum.** The real (solid line) and imaginary (dotted line) parts of the system's eigenvalues are plotted as a function of Ω_p with $\Omega_c = 3 \gamma$ and $\gamma_{\text{eff}} = 3 \gamma$ in cases of (a) $\Omega_{mw} = 0.01 \gamma$, (b) $\Omega_{mw} = 1 \gamma$, (c) $\Omega_{mw} = 2 \gamma$.

parts of the system's eigenvalues as a function of Ω_p , as depicted in Fig. 5. In our parameter space, when the microwave Rabi frequency is $\Omega_{mw} = 0.01 \gamma$ in Fig. 5(a), the relationship between the two levels near the zero energy (blue and red line) are $\text{Re}(E_2) = -\text{Re}(E_3)$ and $\text{Im}(E_2) \neq \text{Im}(E_3)$, indicating that the particle-hole symmetry of the system is completely broken. At $\Omega_{mw} = 1 \gamma$ in Fig. 5(b), it is found that the particle-hole symmetry of the system is spontaneously broken, and the broken defect is at the 'gap-closing' point. However, when the microwave Rabi frequency is $\Omega_{mw} = 2 \gamma$ in Fig. 5(c), the system maintains particle-hole symmetry, and the two eigenvalues have a relationship of $E_2 = -E_3^*$ near the zero energy.

Next, we depict the eigenvalue evolution trajectories in the energy complex plane to reveal the topological phase transition process. When setting $\gamma_{\text{eff}} = 0$ [corresponds to the case of no interaction], the energy complex plane is trivial and there are no imaginary components, see Fig. 6(a). When we set $\Omega_{mw} = 0.01 \gamma$ and $\gamma_{\text{eff}} = 3 \gamma$, the pure non-zero imaginary eigenvalues for E_2 and E_3 (real parts are zero) are observed in Fig. 6(b), highlighting the non-Hermitian nature of the system. The imaginary parts create an additional dissipation, thus inducing a dynamical topological hysteresis trajectory in experiment, as discussed in main text.

From the results depicted in Fig. 6(c), we observe the presence of an exceptional point (EP) where several eigenvalues coalesce simultaneously [this is not observed in Fig. 6(b)]. In Fig. 6(c), the trajectories of E_2 and E_3 exhibit a 'gap-closing' topology in the energy complex plane [8]. This gap-closing behavior signifies a transition between different topological phases, suggesting that the system undergoes critical changes when the parameters are varied. By increasing the microwave Rabi frequency to $\Omega_{mw} = 2 \gamma$, the 'gap-closing' effect is eliminated, as shown in Fig. 6(d). In Fig. 6(d), we can see that the eigenvalues E_2 and E_3 contain both of real and imaginary components.

As illustrated in Figs. 6(b) and (d), the disparity in the real parts of E_2 and E_3 gives rise to two distinctly

different topological hysteresis trajectories in the experiment. In Fig. 6(b), the purely imaginary components contribute to a dynamical hysteresis trajectory characterized by a winding number of $W = -1$. Conversely, under the influence of a strong microwave field, the energy shift of the state $|r\rangle$ becomes significant, leading to the system absorption. This results in an opposite winding number for the trajectory, $W = 1$. Furthermore, in Fig. 6(c), the eigenvalues E_2 and E_3 display a 'gap-closing' spectral behavior. As the driving parameter Ω_p is varied, the spectrum undergoes a transition from possessing real components to becoming entirely imaginary at the EP. This results in the formation of a dynamic hysteresis loop, with a winding number of 1 prior to the EP and -1 following the EP.

Lindblad master equation

By introducing the mean-field term ($\gamma_2 \rightarrow \gamma + V \rho_{rr}$), the Lindblad master equation is written as

$$\dot{\rho}_{gg} = \gamma_1 \rho_{ee} - \frac{1}{2} i (\rho_{ge} - \rho_{eg}) \Omega_p, \quad (6)$$

$$\dot{\rho}_{ge} = \frac{1}{2} i [2 \Delta_1 \rho_{ge} - \rho_{gr} \Omega_c + (\rho_{ee} - \rho_{gg}) \Omega_p + i \gamma_1 \rho_{ge}], \quad (7)$$

$$\dot{\rho}_{gr} = \frac{1}{2} i (\rho_{er} \Omega_p - \rho_{ge} \Omega_c - \rho_{gr} \Omega_{mw} + i \gamma_2 \rho_{gr}) + i (\Delta_1 + \Delta_2) \rho_{gr}, \quad (8)$$

$$\dot{\rho}_{gR} = \frac{1}{2} (-\gamma_3 \rho_{gR} + i \rho_{eR} \Omega_p - i \rho_{gr} \Omega_{mw}) + i (\Delta_1 + \Delta_2 + \Delta_3) \rho_{gR}, \quad (9)$$

$$\dot{\rho}_{ee} = \frac{1}{2} i [\rho_{re} \Omega_c - \rho_{er} \Omega_c + (\rho_{ge} - \rho_{eg}) \Omega_p] + \gamma_2 \rho_{rr} - \gamma_1 \rho_{ee}, \quad (10)$$

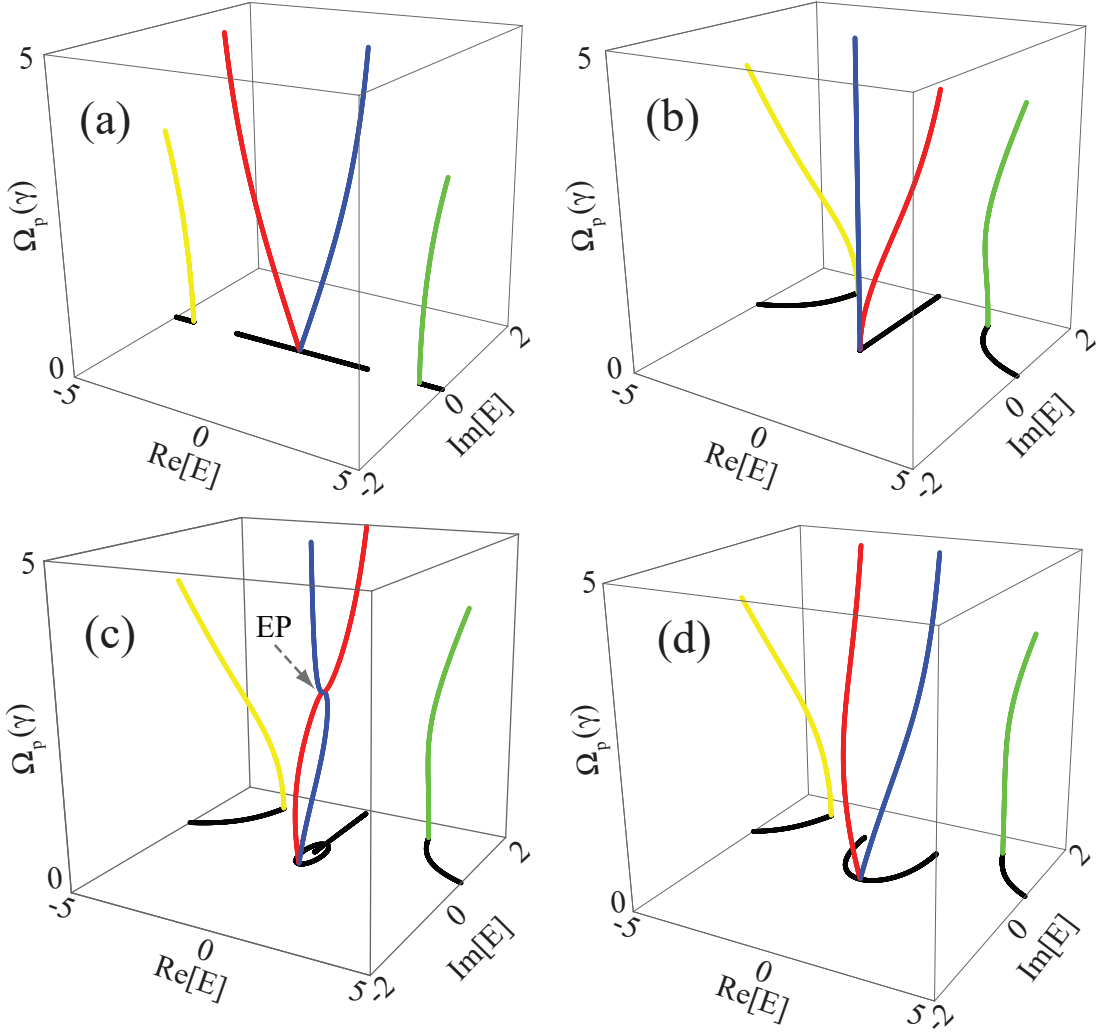


Figure 6. **The eigenvalue trajectories.** The real and imaginary parts of the system's eigenvalues are plotted as a function of Ω_p with $\Omega_c = 3\gamma$ in cases of (a) $\Omega_{mw} = 3\gamma$ and $\gamma_{\text{eff}} = 0$, (b) $\Omega_{mw} = 0.01\gamma$ and $\gamma_{\text{eff}} = 3\gamma$. In (a), there are purely imaginary components on E_2 and E_3 . In (b), the imaginary components are observed. Panels (c) and (d) illustrate the eigenvalue trajectories for the system's eigenvalues at $\Omega_{mw} = \gamma$ and $\gamma_{\text{eff}} = 3\gamma$ (c), $\Omega_{mw} = 2\gamma$ and $\gamma_{\text{eff}} = 3\gamma$ (d). In (c), the curves intersect at an exceptional point (EP), marked by the shaded arrow, where the eigenvalues coalesce. There is a loop closed by the trajectories of E_2 and E_3 . The yellow, red, blue, and green lines correspond to the values of E_1 , E_2 , E_3 , and E_4 , respectively. The black lines refer to the projection of the eigenvalues on the energy complex plane.

$$\begin{aligned} \dot{\rho}_{er} &= \frac{1}{2}i[2\Delta_2\rho_{er} + (\rho_{rr} - \rho_{ee})\Omega_c + \rho_{gr}\Omega_p - \rho_{eR}\Omega_{mw}] \\ &\quad - \frac{1}{2}(\gamma_1 + \gamma_2)\rho_{er}, \end{aligned} \quad (11)$$

$$\begin{aligned} \dot{\rho}_{eR} &= \frac{1}{2}i(2\Delta_2\rho_{eR} + 2\Delta_3\rho_{eR} + \rho_{rR}\Omega_c + \rho_{gR}\Omega_p - \rho_{er}\Omega_{mw}) \\ &\quad - \frac{1}{2}(\gamma_1 + \gamma_3)\rho_{eR}, \end{aligned} \quad (12)$$

$$\begin{aligned} \dot{\rho}_{rr} &= \frac{1}{2}i[\Omega_c(\rho_{er} - \rho_{re}) - \rho_{rR}\Omega_{mw} + \rho_{Rr}\Omega_{mw}] \\ &\quad + \gamma_3\rho_{RR} - \gamma_2\rho_{rr}, \end{aligned} \quad (13)$$

$$\begin{aligned} \dot{\rho}_{rR} &= \frac{1}{2}i[2\Delta_3\rho_{rR} + \rho_{eR}\Omega_c + (\rho_{RR} - \rho_{rr})\Omega_{mw}] - \\ &\quad \frac{1}{2}(\gamma_2 + \gamma_3)\rho_{rR}, \end{aligned} \quad (14)$$

$$\dot{\rho}_{RR} = -\gamma_3\rho_{RR} + \frac{1}{2}i(\rho_{rR} - \rho_{Rr})\Omega_{mw}. \quad (15)$$

The remaining equations are given by $\rho_{eg} = \rho_{ge}^*$, $\rho_{rg} = \rho_{gr}^*$, $\rho_{Rg} = \rho_{gR}^*$, $\rho_{re} = \rho_{er}^*$, $\rho_{Re} = \rho_{eR}^*$, and $\rho_{Rr} = \rho_{rR}^*$. By solving the time-dependent Lindblad master equation outlined above, we obtained the population of the Rydberg state $|r\rangle$. The theoretical results are presented in Fig. 1(c), where we illustrate three dynamical evolution curves of the system at various microwave frequencies Ω_{mw} .

ACKNOWLEDGEMENTS

We acknowledge funding from the National Key R and D Program of China (Grant No. 2022YFA1404002), the National Natural Science Foundation of China (Grant Nos. U20A20218, 61525504, and 61435011), and the Major Science and Technology Projects in Anhui Province (Grant No. 202203a13010001).

DATA AVAILABILITY

All experimental data used in this study are available from the corresponding author upon request.

AUTHOR CONTRIBUTIONS STATEMENT

D.-S.D. conceived the idea. J.Z and Y.J.W conducted the physical experiments. D.-S.D. and Y.J.W developed the theoretical model. The manuscript was written by D.-S.D, J.Z., and Y.J.W. The research was supervised by D.-S.D. All authors contributed to discussions regarding the results and the analysis contained in the manuscript.

COMPETING INTERESTS

The authors declare no competing interests.

-
- [1] S.-Y. Xu, Y. Xia, L. Wray, S. Jia, F. Meier, J. Dil, J. Osterwalder, B. Slomski, A. Bansil, H. Lin, *et al.*, Topological phase transition and texture inversion in a tunable topological insulator, *Science* **332**, 560 (2011).
- [2] M. Caraglio, C. Micheletti, and E. Orlandini, Stretching response of knotted and unknotted polymer chains, *Phys. Rev. Lett.* **115**, 188301 (2015).
- [3] K. Kawabata, S. Higashikawa, Z. Gong, Y. Ashida, and M. Ueda, Topological unification of time-reversal and particle-hole symmetries in non-hermitian physics, *Nat. Commun.* **10**, 297 (2019).
- [4] S. Xia, D. Kaltsas, D. Song, I. Komis, J. Xu, A. Szameit, H. Buljan, K. G. Makris, and Z. Chen, Nonlinear tuning of pt symmetry and non-hermitian topological states, *Science* **372**, 72 (2021).
- [5] W. Ji and X.-G. Wen, Categorical symmetry and noninvertible anomaly in symmetry-breaking and topological phase transitions, *Physical Review Research* **2**, 033417 (2020).
- [6] S.-Y. Xu, C. Liu, N. Alidoust, M. Neupane, D. Qian, I. Belopolski, J. Denlinger, Y. Wang, H. Lin, L. a. Wray, *et al.*, Observation of a topological crystalline insulator phase and topological phase transition in pb1-x sn x te, *Nat. Commun.* **3**, 1192 (2012).
- [7] C. Heide, Y. Kobayashi, D. R. Baykusheva, D. Jain, J. A. Sobota, M. Hashimoto, P. S. Kirchmann, S. Oh, T. F. Heinz, D. A. Reis, *et al.*, Probing topological phase transitions using high-harmonic generation, *Nat. Photonics* **16**, 620 (2022).
- [8] K. Ding, C. Fang, and G. Ma, Non-hermitian topology and exceptional-point geometries, *Nat. Rev. Phys.* **4**, 745 (2022).
- [9] Z. Lin, L. Zhang, X. Long, Y.-a. Fan, Y. Li, K. Tang, J. Li, X. Nie, T. Xin, X.-J. Liu, *et al.*, Experimental quantum simulation of non-hermitian dynamical topological states using stochastic schrödinger equation, *npj Quantum Information* **8**, 77 (2022).
- [10] J. Y. Lee, J. Ahn, H. Zhou, and A. Vishwanath, Topological correspondence between hermitian and non-hermitian systems: Anomalous dynamics, *Phys. Rev. Lett.* **123**, 206404 (2019).
- [11] S. Porta, F. Cavaliere, M. Sasseti, and N. Traverso Ziani, Topological classification of dynamical quantum phase transitions in the xy chain, *Scientific Reports* **10**, 12766 (2020).
- [12] S. Mittal, S. Ganeshan, J. Fan, A. Vaezi, and M. Hafezi, Measurement of topological invariants in a 2d photonic system, *Nat. Photonics* **10**, 180 (2016).
- [13] D. Hao, L. Wang, X. Lu, X. Cao, S. Jia, Y. Hu, and Y. Xiao, Topological atomic spin wave lattices by dissipative couplings, *Phys. Rev. Lett.* **130**, 153602 (2023).
- [14] S. De Léséleuc, V. Lienhard, P. Scholl, D. Barredo, S. Weber, N. Lang, H. P. Büchler, T. Lahaye, and A. Browaeys, Observation of a symmetry-protected topological phase of interacting bosons with Rydberg atoms, *Science* **365**, 775 (2019).
- [15] M. Yang, H.-Q. Zhang, Y.-W. Liao, Z.-H. Liu, Z.-W. Zhou, X.-X. Zhou, J.-S. Xu, Y.-J. Han, C.-F. Li, and G.-C. Guo, Topological band structure via twisted photons in a degenerate cavity, *Nat. Commun.* **13**, 2040 (2022).
- [16] T. Insulator, Topological phase transition and texture inversion in a tunable, *Science* **1201607**, 332 (2011).
- [17] J. Zhang, C.-Z. Chang, P. Tang, Z. Zhang, X. Feng, K. Li, L.-l. Wang, X. Chen, C. Liu, W. Duan, *et al.*, Topology-driven magnetic quantum phase transition in topological insulators, *Science* **339**, 1582 (2013).
- [18] Q. Lin, T. Li, L. Xiao, K. Wang, W. Yi, and P. Xue, Observation of non-hermitian topological anderson insulator in quantum dynamics, *Nat. Commun.* **13**, 3229 (2022).
- [19] G. Zhang *et al.*, Majorana fermions and a topological phase transition in semiconductor-superconductor heterostructures, *Phys. Rev. Lett* **110**, 10 (2013).
- [20] P. Zhang, K. Yaji, T. Hashimoto, Y. Ota, T. Kondo, K. Okazaki, Z. Wang, J. Wen, G. D. Gu, H. Ding, *et al.*, Observation of topological superconductivity on the surface of an iron-based superconductor, *Science* **360**, 182 (2018).
- [21] S. Vajna and B. Dóra, Topological classification of dynamical phase transitions, *Phys. Rev. B.* **91**, 155127 (2015).
- [22] M. Heyl and J. Budich, Dynamical topological quantum phase transitions for mixed states, *Phys. Rev. B.* **96**, 180304 (2017).
- [23] S. Longhi, Topological phase transition in non-hermitian quasicrystals, *Phys. Rev. Lett.* **122**, 237601 (2019).

- [24] T. Dai, Y. Ao, J. Mao, Y. Yang, Y. Zheng, C. Zhai, Y. Li, J. Yuan, B. Tang, Z. Li, *et al.*, Non-hermitian topological phase transitions controlled by nonlinearity, *Nat. Phys.* **20**, 101 (2024).
- [25] Z. Li, L.-W. Wang, X. Wang, Z.-K. Lin, G. Ma, and J.-H. Jiang, Observation of dynamic non-hermitian skin effects, *Nat. Commun.* **15**, 6544 (2024).
- [26] Z. Gong, Y. Ashida, K. Kawabata, K. Takasan, S. Higashikawa, and M. Ueda, Topological phases of non-hermitian systems, *Phys. Rev. X* **8**, 031079 (2018).
- [27] N. Fläschner, D. Vogel, M. Tarnowski, B. Rem, D.-S. Lühmann, M. Heyl, J. Budich, L. Mathey, K. Sengstock, and C. Weitenberg, Observation of dynamical vortices after quenches in a system with topology, *Nat. Phys.* **14**, 265 (2018).
- [28] M. Heyl, Dynamical quantum phase transitions: a review, *Reports on Progress in Physics* **81**, 054001 (2018).
- [29] R. J. Valencia-Tortora, N. Pancotti, M. Fleischhauer, H. Bernien, and J. Marino, Rydberg platform for non-ergodic chiral quantum dynamics, *Phys. Rev. Lett.* **132**, 223201 (2024).
- [30] H.-X. Xiao, W. Jiang, P. Qian, H. Li, Z. Li, H. Shen, and B. Chen, Dynamical topological quantum phase transitions in high-order topological systems, *Phys. Rev. B* **110**, 064306 (2024).
- [31] M. Saffman, T. G. Walker, and K. Mølmer, Quantum information with Rydberg atoms, *Rev. Mod. Phys.* **82**, 2313 (2010).
- [32] C. S. Adams, J. D. Pritchard, and J. P. Shaffer, Rydberg atom quantum technologies, *J. Phys. B: At. Mol. Opt. Phys.* **53**, 012002 (2019).
- [33] A. Browaeys and T. Lahaye, Many-body physics with individually controlled Rydberg atoms, *Nat. Phys.* **16**, 132 (2020).
- [34] R. Samajdar, W. W. Ho, H. Pichler, M. D. Lukin, and S. Sachdev, Quantum phases of rydberg atoms on a kagome lattice, *Proceedings of the National Academy of Sciences* **118**, e2015785118 (2021).
- [35] S. Kanungo, J. Whalen, Y. Lu, M. Yuan, S. Dasgupta, F. Dunning, K. Hazzard, and T. Killian, Realizing topological edge states with rydberg-atom synthetic dimensions, *Nat. Commun.* **13**, 972 (2022).
- [36] K. Li, J.-H. Wang, Y.-B. Yang, and Y. Xu, Symmetry-protected topological phases in a Rydberg glass, *Phys. Rev. Lett.* **127**, 263004 (2021).
- [37] X. Li and S. D. Sarma, Exotic topological density waves in cold atomic rydberg-dressed fermions, *Nat. Commun.* **6**, 7137 (2015).
- [38] R. Verresen, M. D. Lukin, and A. Vishwanath, Prediction of toric code topological order from rydberg blockade, *Phys. Rev. X* **11**, 031005 (2021).
- [39] T. E. Lee, H. Häffner, and M. C. Cross, Collective quantum jumps of Rydberg atoms, *Phys. Rev. Lett.* **108**, 023602 (2012).
- [40] C. Carr, R. Ritter, C. Wade, C. S. Adams, and K. J. Weatherill, Nonequilibrium phase transition in a dilute Rydberg ensemble, *Phys. Rev. Lett.* **111**, 113901 (2013).
- [41] H. Schempp, G. Günter, M. Robert-de Saint-Vincent, C. S. Hofmann, D. Breyel, A. Komnik, D. W. Schönleber, M. Gärttner, J. Evers, S. Whitlock, and M. Weidemüller, Full counting statistics of laser excited Rydberg aggregates in a one-dimensional geometry, *Phys. Rev. Lett.* **112**, 013002 (2014).
- [42] M. Marcuzzi, E. Levi, S. Diehl, J. P. Garrahan, and I. Lesanovsky, Universal nonequilibrium properties of dissipative Rydberg gases, *Phys. Rev. Lett.* **113**, 210401 (2014).
- [43] I. Lesanovsky and J. P. Garrahan, Out-of-equilibrium structures in strongly interacting Rydberg gases with dissipation, *Phys. Rev. A* **90**, 011603 (2014).
- [44] A. Urvoy, F. Ripka, I. Lesanovsky, D. Booth, J. Shaffer, T. Pfau, and R. Löw, Strongly correlated growth of Rydberg aggregates in a vapor cell, *Phys. Rev. Lett.* **114**, 203002 (2015).
- [45] D.-S. Ding, Z.-K. Liu, B.-S. Shi, G.-C. Guo, K. Mølmer, and C. S. Adams, Enhanced metrology at the critical point of a many-body Rydberg atomic system, *Nat. Phys.* **18**, 1447 (2022).
- [46] S. Helmrich, A. Arias, G. Lochead, T. M. Wintermantel, M. Buchhold, S. Diehl, and S. Whitlock, Signatures of self-organized criticality in an ultracold atomic gas, *Nature* **577**, 481 (2020).
- [47] D.-S. Ding, H. Busche, B.-S. Shi, G.-C. Guo, and C. S. Adams, Phase diagram of non-equilibrium phase transition in a strongly-interacting Rydberg atom vapour, *Phys. Rev. X* **10**, 021023 (2020).
- [48] T. M. Wintermantel, Y. Wang, G. Lochead, S. Shevate, G. K. Brennen, and S. Whitlock, Unitary and nonunitary quantum cellular automata with Rydberg arrays, *Phys. Rev. Lett.* **124**, 070503 (2020).
- [49] K. Klocke, T. Wintermantel, G. Lochead, S. Whitlock, and M. Buchhold, Hydrodynamic stabilization of self-organized criticality in a driven Rydberg gas, *Phys. Rev. Lett.* **126**, 123401 (2021).
- [50] F. M. Gambetta, F. Carollo, M. Marcuzzi, J. P. Garrahan, and I. Lesanovsky, Discrete time crystals in the absence of manifest symmetries or disorder in open quantum systems, *Phys. Rev. Lett.* **122**, 015701 (2019).
- [51] K. Wadenpfuhl and C. S. Adams, Emergence of synchronization in a driven-dissipative hot Rydberg vapor, *Phys. Rev. Lett.* **131**, 143002 (2023).
- [52] D. Ding, Z. Bai, Z. Liu, B. Shi, G. Guo, W. Li, and C. S. Adams, Ergodicity breaking from Rydberg clusters in a driven-dissipative many-body system, *Science advances* **10**, ead15893 (2024).
- [53] X. Wu, Z. Wang, F. Yang, R. Gao, C. Liang, M. K. Tey, X. Li, T. Pohl, and L. You, Dissipative time crystal in a strongly interacting Rydberg gas, *Nat. Phys.* , 1 (2024).
- [54] B. Liu, L.-H. Zhang, Z.-K. Liu, J. Zhang, Z.-Y. Zhang, S.-Y. Shao, Q. Li, H.-C. Chen, Y. Ma, T.-Y. Han, *et al.*, Higher-order and fractional discrete time crystals in floquet-driven Rydberg atoms, *arXiv preprint arXiv:2402.13657* (2024).
- [55] B. Liu, L.-H. Zhang, Z.-K. Liu, J. Zhang, Z.-Y. Zhang, S.-Y. Shao, Q. Li, H.-C. Chen, Y. Ma, T.-Y. Han, *et al.*, Bifurcation of time crystals in driven and dissipative Rydberg atomic gas, *arXiv preprint arXiv:2402.13644* (2024).
- [56] B. Liu, L.-H. Zhang, Y. Ma, T.-Y. Han, Q.-F. Wang, J. Zhang, Z.-Y. Zhang, S.-Y. Shao, Q. Li, H.-C. Chen, *et al.*, Microwave seeding time crystal in floquet driven Rydberg atoms, *arXiv preprint arXiv:2404.12180* (2024).
- [57] P. Delplace, T. Yoshida, and Y. Hatsugai, Symmetry-protected multifold exceptional points and their topological characterization, *Phys. Rev. Lett.* **127**, 186602 (2021).

- [58] J. Zhang, E.-Z. Li, Y.-J. Wang, B. Liu, L.-H. Zhang, Z.-Y. Zhang, S.-Y. Shao, Q. Li, H.-C. Chen, Y. Ma, *et al.*, Exceptional point and hysteresis trajectories in cold Rydberg atomic gases, [arXiv preprint arXiv:2408.03109 \(2024\)](#).